Neuron

NeuroResource

Magnetoelectric Materials for Miniature, Wireless Neural Stimulation at Therapeutic Frequencies

Graphical Abstract

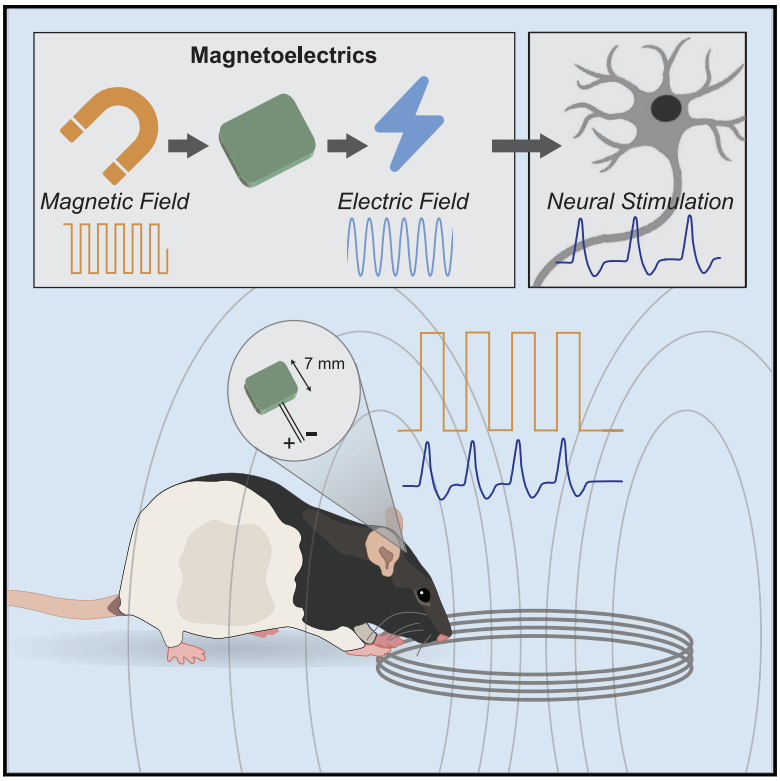

Authors

Amanda Singer, Shayok Dutta, Eric Lewis, ..., Michael Beierlein, Caleb Kemere, Jacob T. Robinson

Correspondence

jtrobinson@rice.edu

In Brief

Magnetoelectric (ME) materials enable tiny remotely powered neural stimulators. Singer et al. demonstrate that alternating magnetic fields can power millimeter-sized ME stimulators in freely moving rodents. The extreme miniaturization made possible by this technology lays the foundation for a new class of minimally invasive bioelectronics.

Highlights

- Magnetoelectric materials enable millimeter-sized wireless stimulators
- Wireless neural stimulators reach therapeutic frequencies in freely moving rodents
- Miniature bioelectronic devices treat Parkinson's disease in a rat model

Singer et al., 2020, Neuron *107*, 631–643
August 19, 2020
https://doi.org/10.1016/j.neuron.2020.05.019

CellPress

Neuron

CellPress

NeuroResource

Magnetoelectric Materials for Miniature, Wireless Neural Stimulation at Therapeutic Frequencies

Amanda Singer,[1,2] Shayok Dutta,[2] Eric Lewis,[2] Ziying Chen,[2] Joshua C. Chen,[3] Nishant Verma,[3] Benjamin Avants,[2] Ariel K. Feldman,[4,5] John O'Malley,[6] Michael Beierlein,[6] Caleb Kemere,[2,3] and Jacob T. Robinson[1,2,3,7,8,*]

[1]Applied Physics Program, Rice University, Houston, TX 77005, USA
[2]Department of Electrical and Computer Engineering, Rice University, Houston, TX 77005, USA
[3]Department of Bioengineering, Rice University, Houston, TX 77005, USA
[4]Department of Computer Science, Rice University, Houston, TX 77005, USA
[5]Department of Cognitive Science, Rice University, Houston, TX 77005, USA
[6]Department of Neurobiology and Anatomy, McGovern Medical School at UTHealth, Houston, TX 77030, USA
[7]Department of Neuroscience, Baylor College of Medicine, Houston, TX 77030, USA
[8]Lead Contact
*Correspondence: jtrobinson@rice.edu
https://doi.org/10.1016/j.neuron.2020.05.019

SUMMARY

A major challenge for miniature bioelectronics is wireless power delivery deep inside the body. Electromagnetic or ultrasound waves suffer from absorption and impedance mismatches at biological interfaces. On the other hand, magnetic fields do not suffer these losses, which has led to magnetically powered bioelectronic implants based on induction or magnetothermal effects. However, these approaches have yet to produce a miniature stimulator that operates at clinically relevant high frequencies. Here, we show that an alternative wireless power method based on magnetoelectric (ME) materials enables miniature magnetically powered neural stimulators that operate up to clinically relevant frequencies in excess of 100 Hz. We demonstrate that wireless ME stimulators provide therapeutic deep brain stimulation in a freely moving rodent model for Parkinson's disease and that these devices can be miniaturized to millimeter-scale and fully implanted. These results suggest that ME materials are an excellent candidate to enable miniature bioelectronics for clinical and research applications.

INTRODUCTION

Wireless neural stimulators have the potential to provide less invasive, longer lasting interfaces to brain regions and peripheral nerves than battery-powered or wired stimulators. Batteries increase the size and weight of an implant and can require replacement or charging; percutaneous and implanted wires present a pathway for infection (Hargreaves et al., 2004) and limit the ability of stimulators to move with the tissue, leading to a foreign body response or loss of contact with the target tissue (Biran et al., 2007; Markwardt et al., 2013). Additionally, chronic fatigue on wires can lead to failure in the wire itself or its connection to the stimulator (Sahin and Pikov 2011). In rodents, wires used to power neural stimulators can interfere with behavior, particularly when studying social interaction between animals (Pinnell et al., 2018).

A primary challenge for wireless neural stimulators is to create efficient miniature devices with cross-sections roughly the size of a grain of rice (<25 mm^2 in area) that operate reliably beneath bone and tissue as an animal or human patient engages in normal activity; however, for devices this small, power delivery remains a challenge. Power transfer with electromagnetic (EM) waves requires antennas with feature sizes comparable to the EM wavelength. Thus, for sub-millimeter devices, such as radio frequency (RF) powered "neurograins,"(Nurmikko 2018) effective frequencies lie in the GHz range, where EM radiation is absorbed by the body. This limits the power that can be safely delivered to implants deep in tissue and often requires device placement to be near the surface of the skin (IEEE 2006). As a result, researchers typically turn to near-field inductive coupling (NIC) to power implanted devices, but this also has miniaturization limits. When the receiver coils are miniaturized, the output power reduces due to the decrease in captured flux and becomes more sensitive to perturbations in the distance or angle between the transmitter and receiver (Fotopoulou and Flynn 2011). For example, Freeman et al. (2017) demonstrated that small inductive coils less than 1 mm in diameter can power stimulators for the sciatic nerve in anesthetized rats; however, stable performance has been difficult to achieve in freely moving animals due to changes in the angle and distance between the receiver and transmitter during behavior (Maeng et al., 2019). NIC has also been used to power optogenetic stimulators in freely moving mice (Shin et al., 2017), which is highly effective when the coils are at or near the surface of the skin. But, the

relatively large cross-sectional area (70 mm^2) of the receiving coil and sensitivity to coil curvature could limit its application for implants that are deep inside the body.

Additionally, many therapeutic applications require high-frequency stimulation, which has been difficult to achieve with miniature bioelectronic devices. Many disorders like Parkinson's Disease (PD) and obsessive-compulsive disorder require stimulators in the high-frequency "therapeutic band" between 100 and 200 Hz (de Hemptinne et al., 2015; Alonso et al., 2015; Theodore and Fisher 2004). This frequency of stimulation is challenging because charge on an electrode must be dissipated between successive stimulation pulses to prevent electrolysis, tissue damage, and changes to the local pH (Merrill et al., 2005). All clinically approved electrical neural stimulation therapies in this therapeutic band use various forms of "charge balanced" biphasic stimulation waveforms that actively or passively charges and discharges the electrode with each cycle (Parastarfeizabadi and Kouzani 2017).

Recently, several new wireless technologies have enabled miniature neural stimulators; however, these approaches have yet to demonstrate high-frequency stimulation in freely moving animals. Researchers have shown that the mouse body can be used as an EM resonant cavity to transfer energy to sub-wavelength-scale devices implanted inside the animal (Montgomery et al., 2015; Ho et al., 2015). This technique has also been used with conformal phase surfaces to activate devices in larger animals (Agrawal et al., 2017). Although this approach is effective for driving LEDs for optogenetic stimulation in mice, monophasic electrical stimulation has been limited to <20 Hz and would require the use of active programmable integrated circuits to safely access higher frequencies and individually address multiple motes. Using superparamagnetic nanoparticles to absorb energy from alternating magnetic fields (500 kHz) (Carrey et al., 2011), one can heat specific regions of the brain (Chen et al., 2015; Munshi et al., 2017) in freely moving mice (Munshi et al., 2017). This stimulates neural activity when the targeted brain area is genetically modified to respond to temperature changes (Chen et al., 2015; Munshi et al., 2017). However, this transgenic method adds regulatory complexity and has yet to show high-frequency operation due the need for the tissue to cool between stimulation pulses. Ultrasound provides an efficient method to power implants because the wavelengths are 10^5 times smaller than EM waves at the same frequency, allowing for miniature piezoelectric antennas (Johnson et al., 2018; Seo et al., 2016; Piech et al., 2020). However, using these "StimDust" motes is challenging and has not yet been demonstrated in freely moving animals because the impedance mismatches require contact between soft tissue and the ultrasound transducer for efficient power transfer. For a more detailed comparison of these current technologies see Table 1.

Here, we show that magnetoelectric (ME) materials enable magnetically powered miniature neural stimulators that operate across low and high therapeutic frequencies. Similar to inductive coils, these materials transform a magnetic field to an electric field, but by mechanical coupling between magnetostrictive and piezoelectric layers in a thin film. The magnetic field generates strain in the magnetostrictive layer as the magnetic dipoles align with the applied field. That strain exerts a force on the piezoelectric layer, which generates a voltage (Figure 1). By exploiting this mechanism, MEs do not suffer from the same miniaturization constraints as coils and can be driven by weak magnetic fields on the order of a few millitesla (mT). These properties have led researchers to propose MEs as a promising material for bioelectronic implants (Nan et al., 2017; O'Handley et al., 2008; Yue et al., 2012; Guduru et al., 2015; Ribeiro et al., 2016). We demonstrate proof-of-principle wireless neural stimulators based on ME materials and show that they effectively treat the symptoms of PD in a freely behaving rodent disease model. We further show that ME materials can be miniaturized to the size of a grain of rice, fully implanted under the skin, and effectively stimulate the brain of freely behaving rodents to drive a place preference.

RESULTS

Fabrication and Characterization of ME Stimulators

We fabricated miniature ME stimulators (Figures 1A and 1C) by bonding a rectangular magnetostrictive layer (Metglas) to a piezoelectric layer, polyvinylidene fluoride (PVDF) or lead zirconate titanate (PZT), before encapsulating the films with parylene-C (8–10 um). (Figure 1B; see STAR Methods). We used PVDF or PZT layers between 28 and 110 μm, which yielded total device thicknesses between 50–150 μm. We found a dramatic increase in the voltage measured across the film when the applied magnetic field frequency matches an acoustic resonant frequency (Figure 1D). Because the resonant frequency is proportional to the inverse of the film length (Figure S1I), we can design multiple films and selectively activate them by changing the stimulus frequency. Using this principle, we can use different magnetic field frequencies to activate separate monophasic devices that may be in different areas of the body or create biphasic stimulators by interleaved resonant stimulation of two different films, with each film driving either the positive or negative phase of the neural stimulus.

We can further enhance the voltage generated by the films by applying a constant bias field with a permanent magnet or an electromagnet (Figure 1E). Because the strain in the magnetostrictive material is a sigmoidal function of the magnetic field strength, the change in voltage produced by the alternating field is largest when the field oscillates about the midpoint of the sigmoid (Figures S1A–S1C; Zhai et al., 2006; Kulkarni et al., 2014). Thus, we use a bias field (approximately 8–9 mT for devices used here) to offset the alternating magnetic field near the center of the sigmoidal magnetostrictive response curve. Our references to magnetic field strength in this work refer to the amplitude of the alternating magnetic field around this bias point.

To identify safe operational conditions for our ME stimulators, we tested them using a stereotrode (Microprobes) in saline over a range of frequencies (see STAR Methods). We found that a biphasic stimulation waveform allowed us to apply constant stimulation up to at least 800 Hz without hydrolysis and that monophasic stimulation could be safely applied up to approximately 50 Hz. For these tests, we used a stimulation amplitude of 2 V and a duration of 400 μs/phase (which is common for *in vivo* experiments). The safe ranges were determined by measuring the time at which we could see bubbles at the electrode tip (Figure 1F) resulting from hydrolysis, which indicates conditions that would lesion tissue. Compared to previously demonstrated

Table 1. Comparison of Miniature Neural Stimulators

Technology	Inductive Optogenetics	E-Particle	Mid-Field	Mid-Field	Stim Dust	RF Antenna	Magneto Thermal 1	Magneto Thermal 2	This Work Demo 1	This Work Demo 2
Reference[a]	[a]	[b]	[c]	[d]	[e]	[f]	[g]	[h]	This work	This work
Power type (implant)	Inductive coil	Inductive coil	Mid-field coil	Mid-field coil	Piezo electric	RF antenna	Nano-particle injection	Nano-particle injection	Magneto electric	Magneto electric
Activation by:	Magnetic field	Magnetic field	Electro magnetic	Electro magnetic	Ultra-sound	Electro magnetic	Magnetic field	Magnetic field	Magnetic field	Magnetic field
Carrier frequency	13.56 MHz	10.9 MHz	1.5 GHz	1.6 GHz	1.85 MHz	2.3-3.2 GHz	500 kHz	500 kHz	100–170 kHz	250–400 kHz
Stimulation type	LED	Electrical	LED	Electrical	Electrical	LED	Heat	Heat	Electrical	Electrical
Whole implant size (mm^3)	100	0.5	10–25	15	6.5	24	N/A	N/A	500	175
Size of power source (mm^3)	40	0.25	5	5	~0.5	20	N/A	N/A	20	2–4
Implant weight (mg)	30		25–50	70	10	33			500	500
Max implant power (in animal, mW)	30	0.036[b]	10	2	0.35		N/A	N/A	0.1–0.2	2
Demonstrated charge balance (y/n)	N/A	No	N/A	No	Yes	N/A	N/A	N/A	Yes	Yes
Freely moving (y/n)	Yes	Yes	Yes	No	No	Yes	No	Yes	Yes	Yes
Arena volume (cm^3)	12,000	1,000[b]	1,000	N/A	N/A	Video tracked area	N/A	300	3,000–7,000	500
Magnetic field strength (mT)		0.04					19	9.4	1–2	1–2
Genetic modification (y/n)	Yes	No	Yes	No	No	Yes	Yes	Yes	No	No
Fully implanted (y/n)	Yes	Yes	Yes	Yes	Yes	Yes	Yes	Yes	No	Yes
Stimulation frequency (Hz)		50		~3	2 khz		<1 (0.02)	<1 (0.005)	200	150
Required power (W)			4					7500	30	7

N/A, not applicable
[b]Estimated based on published data
[a]References: [a], Shin et al. (2017); [b], Freeman et al. (2017), Maeng et al. (2019); [c], Montgomery et al. (2015); [d], Ho et al. (2015); [e], Piech et al. (2020); [f], Park et al. (2016); [g], Chen et al. (2015); [h], Munshi et al. (2017)

miniature magnetic neural stimulators that operated in a monophasic stimulation mode, the biphasic ME devices shown here can access the high-frequency bands used for clinical applications like the treatment of PD and obsessive-compulsive disorder (Figure 1F). The ME devices can also operate safely in a monophasic mode for low-frequency applications, such as heart pacing or chronic pain stimulators, which can be achieved with a simplified ME device. One should note that the exact safety windows depend on the amplitude, duty cycle, and electrode configuration of the stimulator.

An additional challenge for any wirelessly powered neural stimulator is to maintain a well-regulated stimulation voltage, especially as devices become small and the power transfer efficiency is reduced. ME materials offer two main advantages that can enable stable and effective stimulation as devices become small and move with respect to the driver coils.

First, ME devices generate voltages in excess of the effective stimulation potential, allowing them to be effective even if the materials are misaligned with the driver coils. At resonance, we have measured open-circuit ME voltages in excess of 30 V at a field strength of only 1 mT (Figures S1K and S1M). Because effective stimulation voltages are usually between 1–5 V, we can cap the applied voltage to this effective stimulation range using an LED or Zener diode. As long as the voltage generated by the ME film is greater than or equal to the capping voltage, our device could apply the same stimulus voltage regardless of the angle or distance between the driver coil and the ME film. For a typical film, we found that we could reorient the film by ±80 degrees and maintain voltages in excess of 3 V (Figure S1D). This large angular tolerance is aided by the large magnetic permeability of the Metglas layer, which helps to direct the magnetic field lines along the long axis of the film, where they are most effective at creating a magnetostrictive response.

Second, the voltage generated by a piezoelectric material depends on the thickness and not the area of the piezoelectric layer (Wan and Bowen 2017), allowing us to fabricate small ME films

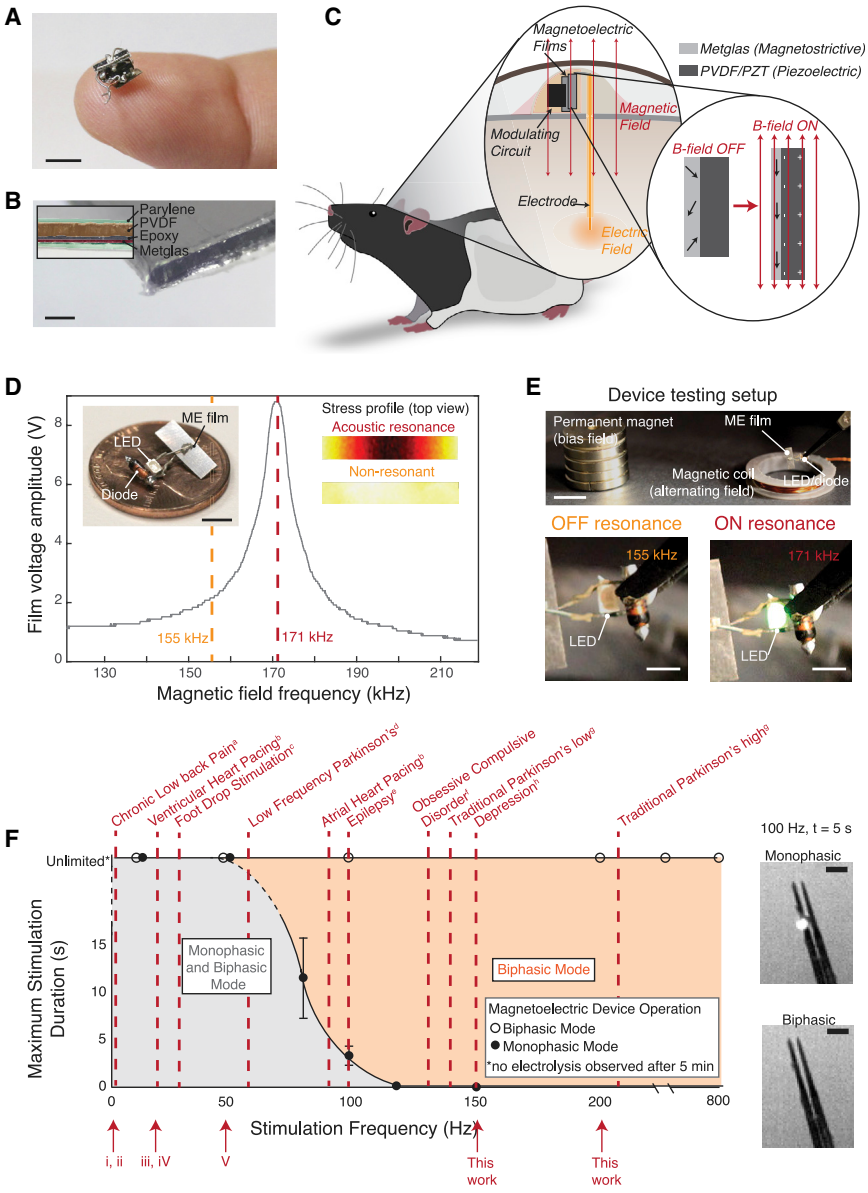

Figure 1. ME Films Convert Alternating Magnetic Fields into a Voltage

(A) Photo of a ME device shown on a fingertip; scale bar, 5 mm.

(B) Cross-sectional image of a cut ME film; scale bar, 0.2 mm.

(C) Diagram of a ME device on a freely moving rat for wireless neural stimulation. Inset shows the operating principle whereby strain in the magnetostrictive layer is transferred to the dark gray piezoelectric layer, creating a voltage across the film.

(D) Example of a resonant response curve for a ME film where the maximum voltage is produced at an acoustic resonance at 171 kHz. Photograph inset shows an example of an assembled ME stimulator; scale bar, 5 mm. "Stress profile" inset shows a top view of the stress produced in a ME film, as calculated by a finite element simulation ON and OFF resonance (COMSOL).

(E) Device testing setup with a permanent magnet to apply a bias field and an electromagnetic coil to apply an alternating magnetic field; scale bars, top = 1 cm, bottom = 2 cm.

(F) Maximum stimulation duration for a ME device in biphasic and monophasic operation determined by time of electrolysis on a stereotrode in saline, as evidenced by gas bubbles (error bars ± 1 standard deviation for n = 4 trials); scale bars, 0.2 mm. Dashed red lines indicate frequencies of electrical stimulation used in clinical applications; a: Schabrun et al. (2014), b: Mulpuru et al. (2017), c: Kesar et al. (2010), d: Baizabal-Carvallo and Alonso-Juarez (2016), e: Theodore and Fisher (2004), f: Alonso et al. (2015), g: de Hemptinne et al. (2015), h: Bewernick et al. (2010). Roman numerals indicate stimulation frequencies demonstrated by previously published miniature magnetic stimulators; i: Chen et. al. (2015), ii: Munshi et. al. (2017), iii: Montgomery et. al. (2015), iv: Freeman et. al. (2017) v: Maeng et. al. (2019). See also Figure S1.

that generate roughly the same stimulation voltage as larger devices. Figures S1J and S1K show the peak voltage generated and quality factor for ME films of different areas. We found that for a 52-μm-thick PVDF layer, the voltage remains around 10 V even as the film length decreases. Variations of ±40% in peak voltage and quality factors are likely due to defects produced during film fabrication, which may be reduced with improved manufacturing. We also verified that the output voltage depends only on the piezoelectric film thickness by measuring the peak voltages from ME devices with three different thicknesses of PVDF: 28 μm, 52 μm, and 110 μm. As expected, we see that the peak voltage increases linearly with the PVDF thickness and is independent of the film length.

For applications such as current delivery through implanted electrodes, where the available power is an important figure of merit, the advantage of our ME technology is the power we get from a millimeter-sized magnetically powered device. This allows us to perform experiments that require high power like high-frequency biphasic stimulation. Our calculations and experimental data show that the power generated by a ME device is proportional to the film area for a given thickness and a length-to-width ratio of >3 (see Figure S1L). This output power is also dependent on the d_{31} coefficient of the piezoelectric material (Figure S1). Despite the decrease in power as films become smaller, we calculate that PVDF and Metglas films less than 10 mm long can generate up to 4 mW, which is sufficient for many wireless applications, including neural stimulation (Ben Amar et al., 2015). In applications requiring higher power at miniature scales, we use PZT and Metglas ME films due to the higher d_{31} of PZT.

Monophasic Stimulation by ME Films Modulates Cellular Activity *In Vitro*

Using fluorescence microscopy to image voltage in cultured cells, we found that monophasic stimulation directly from PVDF and Metglas ME films reliably stimulated action potentials (APs). For these experiments, we used "spiking" human embryonic kidney (HEK) cell lines that were modified to express sodium and potassium channels (see STAR Methods). These cells have spike-like electrical waveforms that are rectangular in shape and can last for a few seconds depending on the confluency of the culture (Park et al., 2013). To determine the relative timing between magnetic stimulation and AP generation, we transfected these cells with ArcLight (Jin et al., 2012), a genetically encoded voltage indicator.

To image fluorescence while we applied magnetic fields, we developed an experimental setup that allows us to place cells and ME films beneath an objective lens at the center of a 10-cm-long solenoid with a 3-cm gap in the center (Figure 2A). The field strengths (<1 mT; Figure S2F) and frequencies (20–40 kHz) used in this experiment did not produce noticeable heat in our metallic objective lens or interfere with our imaging. Two slightly larger coils placed on either side of the gap provided the constant bias field.

We then approximated an implanted the ME stimulator by using two experimental configurations: (1) growing cells directly on the ME film (Figure S2) and (2) inverting a coverslip with adherent cells on top of the ME film (Figure 2) because in a typical use case, the target cells may not adhere to the ME stimulator (see STAR Methods).

To create fringing electric fields that interact with the cultured cells, we stamped holes in the ME film (Figure 2B). The films were otherwise fabricated as described above (Figure 1; STAR Methods). In experiments using ME films and platinum electrodes, we found that high-frequency biphasic stimulation at the ME resonance frequency (typically 20–150 kHz) was not effective to stimulate APs in cultured HEKs, as predicted by the low-pass filtering properties of the cell membrane (Freeman et al., 2017). To create an effective monophasic stimulus waveform, we used a diode to rectify the voltage to generate a waveform that has a slowly varying monophasic envelope in the <500-Hz frequency band where cells are responsive (Figures 2C and 2D).

For cells grown directly on the ME films and those placed in contact, we found that five stimulation pulses with an envelope frequency of 100 Hz (applied for only 50 ms total so as not to introduce hydrolysis) consistently stimulated APs in the spiking HEK cells (Figures 2E and S2D; Video S1). Critically, this stimulation frequency is within the therapeutic window for many deep brain stimulation (DBS) treatments (So et al., 2017) and is difficult to achieve with other wireless stimulators that compensate for low-efficacy energy harvesting by charging on-board capacitors (Sun et al., 2017). For our experiments, the carrier frequency of the magnetic field was at the resonant frequency of the film (Figure S2C). To test stimulation reliability, we repeated the 5-pulse stimulus three times over a period of 30 s. We observed APs for each stimulation pulse in n = 43 cells on coverslips and n = 144 cells grown on films. In these experiments, all cells in the field of view were activated simultaneously due to the fact that HEK cells are known to be electrically coupled when grown to confluence (Park et al., 2013). We confirmed that the APs stimulated by the ME film were, in fact, the result of resonant excitation of the film and not an artifact of the applied magnetic fields by imaging voltage-sensitive fluorescence when the magnetic field was tuned off of the resonant frequency. For non-resonant excitation, we observed no correlation between the applied field and fluorescently detected APs in the spiking HEKs (Figures 2F and S2E), supporting the conclusion that APs were stimulated by the ME film at resonance. We also confirmed that the fluorescent signal recorded represents the voltage-dependent ArcLight response by imaging cells transfected with voltage-independent cytoplasmic GFP. These cells showed no change in fluorescence when the films were driven at the resonant frequency (Figure 2G).

ME Devices Can Be Individually Addressed Based on Their Resonant Frequency

Another advantage of ME technology is that we can individually address multiple miniature implanted devices by fabricating the films to have unique resonant frequencies. As a demonstration, we show that two rice-sized ME films with cross-sectional areas of $\sim$16 mm^2 can be individually addressed at the center of a human skull phantom by using an external electromagnet. These films with lengths of 8 mm and 10 mm have resonant frequencies of 180 and 200 kHz (Figure 2H). When they are attached to an orange LED, their output voltage is capped at 1.8 V, which allows us to regulate the stimulation voltage and visualize film activation. ME films of this size are smaller than current DBS leads and could potentially be implanted into deep brain areas, as shown in Figures 2I–2L. Additionally, the magnetic coil is small enough to be incorporated into a stylish hat that could be worn by a patient. When we placed the two ME films at the center of a skull phantom, we could individually light the LEDs on each film when we applied a magnetic field (0.5 mT at the center of the skull phantom) at the resonant frequency of the selected film (Figures 2I–2L). The skull top was removed for visualization but had no effect on our ability to drive the LEDs. The number of stimulation channels could be increased with the addition of ME films with different resonant frequencies.

Biphasic Stimulation from ME Films Can Drive High-Frequency Neural Activity *Ex Vivo*

Biphasic stimulation is used for most biomedical stimulators because its charge-balanced waveform reduces charge buildup and undesired electrochemical reactions at the electrode surface (Merrill et al., 2005). To create an effective biphasic stimulus in the therapeutic window (100–200 Hz), we use two films with distinct resonant frequencies connected to the same stimulating electrodes (Figures 3A and 3C). By switching the magnetic field frequency between the two resonant frequencies, we can alternate positive and negative phase stimulation to create a biphasic neural stimulator (Figures 3D and 3E). In this case, the residual charge of <1 nC, which discharges in <2 ms, implies that this stimulator can safely operate at frequencies up to >500 Hz without accumulating charge.

We demonstrated that clinically relevant regions of high-frequency stimulation are safely accessible with this ME-powered

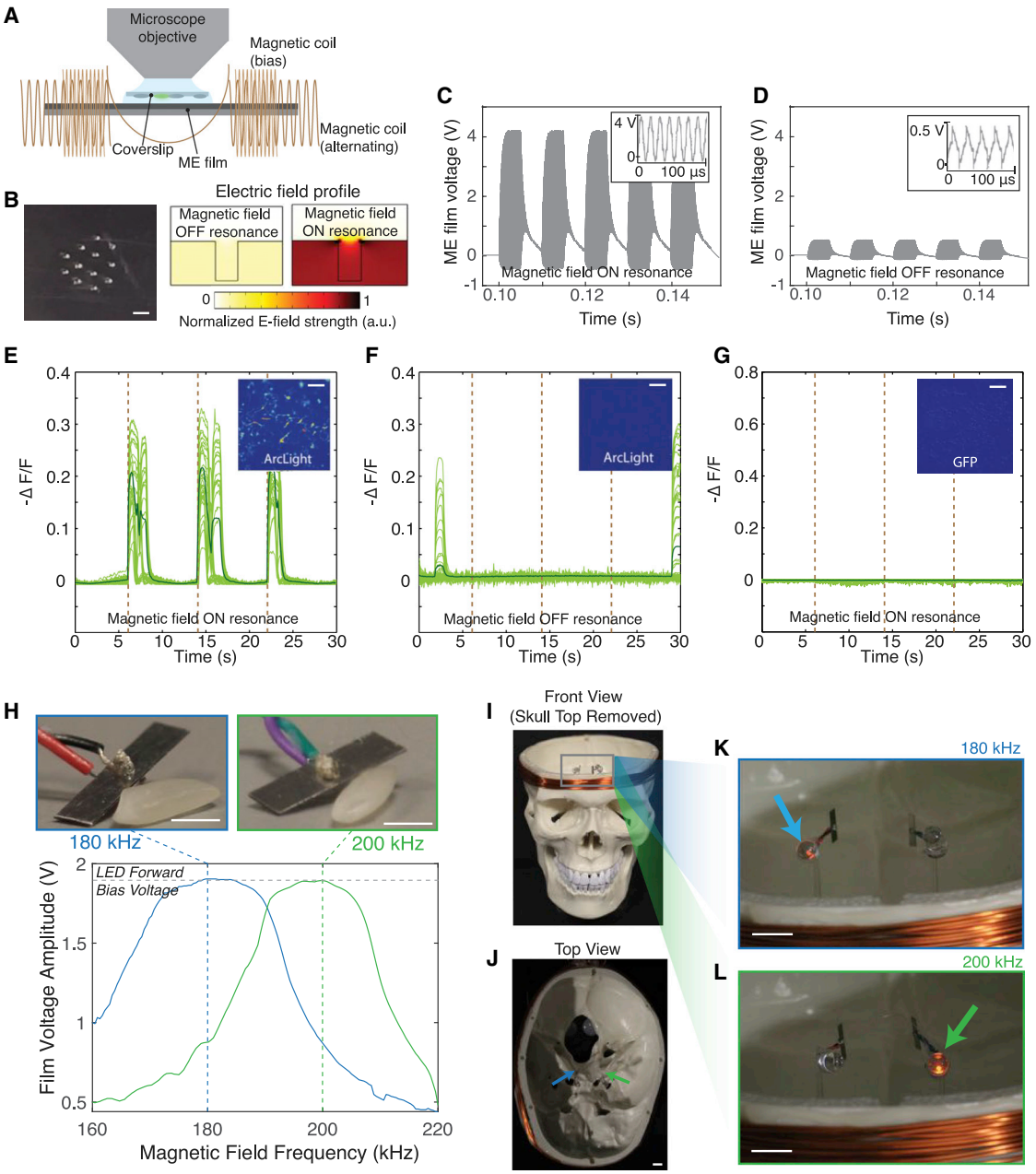

Figure 2. Monophasic ME Stimulators Activate Cells *In Vitro*

(A) Schematic of the experimental setup.

(B) Microscope image of holes stamped into the ME film (scale bar, 0.5 mm), and finite element simulation of the electric field shows fringing electric fields that overlap the culture cells.

(C and D) Voltage across the ME film when the magnetic field is ON resonance (C) and OFF resonance (D). Insets show a zoom in of the high-frequency carrier waveform.

(E–G) Fluorescence from spiking HEKs transfected with ArcLight show action potentials are triggered by the ME film driven at resonance (E) but not when the film is driven OFF resonance (F). Fluorescence from HEK cells transfected with GFP (G) show no response when the ME film is driven ON resonance; scale bars, 0.2 mm.

(H) Photos of miniature ME films next to a grain of rice and the corresponding voltage as a function of magnetic field frequency (field strength, 0.5 mT; scale bars, 2 mm).

(I and J) Front view (I) and top view (J) of skull phantom with the top removed to view LEDs (film locations indicated by arrows; scale bar, 1 cm.

(K and L) Photo of LEDs attached to ME films with the magnetic fields at applied at 180 kHz (K) and 200 kHz (L). Selective illumination of the LEDs corresponding the resonant frequencies of the films demonstrates successful multichannel activation of individual films; scale bars, 1 cm. See also Figures S2 and S6 and Video S1.

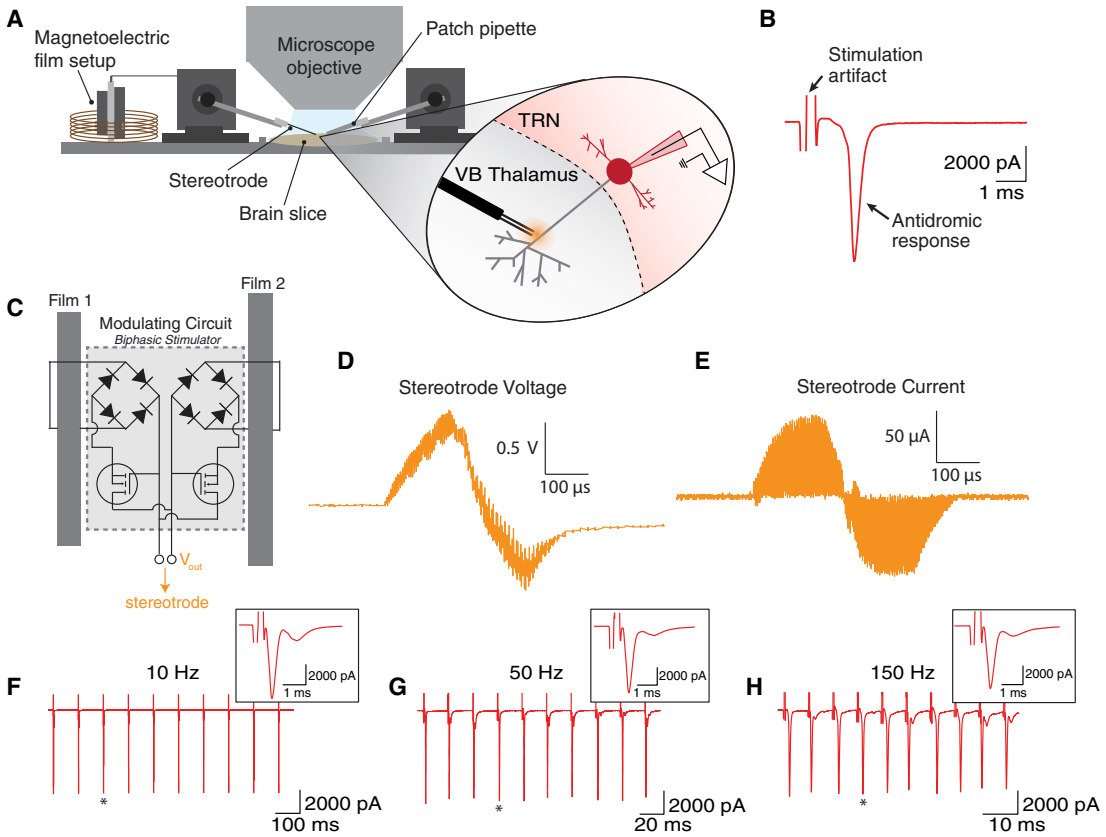

Figure 3. Biphasic ME Stimulators Activate Neurons in *Ex Vivo* Brain Slices

(A) Schematic of experimental setup with two ME films for biphasic stimulation. A bipolar stereotrode was placed into the ventrobasal nucleus of the thalamus to activate axons of TRN neurons.

(B) Representative voltage-clamp recording in TRN showing stimulation-triggered short-latency antidromic spike (stimulus artifact cropped for clarity).

(C) Schematic of the circuit used to generate the biphasic waveform.

(D) Measured voltage across the stereotrode shows the biphasic pulse shape.

(E) Calculated current based on measuring the voltage across a load resistor shows nearly perfect charge balancing with <1 nC accumulating on the electrode per pulse train.

(F–H) Recorded spike activity at various frequencies of ME stimulation demonstrates the ability of the ME device to reliably entrain action potential activity at 10 (F), 50 (G), and 150 Hz (H) (stimulus artifacts cropped for clarity); insets show zoom in of individual antidromic spikes. See also Figure S3.

device by using our biphasic ME stimulator to drive high-frequency neural spikes in a mouse brain slice (see STAR Methods). We stimulated axons of thalamic reticular nucleus (TRN) neurons by placing a stereotrode attached to the ME stimulator into the adjacent ventrobasal nucleus of the thalamus and performing whole-cell voltage-clamp recordings in TRN neurons (Figure 3A). We found that short-latency antidromic spikes were reliably evoked (Figure 3B), with the recorded spike frequency matching the programmed magnetic field envelope frequency (10, 50, and 150 Hz) confirming that neuronal activity can be precisely controlled using our ME stimulation (Figures 3F–3H).

We also found that our biphasic ME stimulator is capable of repeatable neural stimulation using neocortical brain slices derived from mice that express the genetically encoded calcium indicator GCaMP3 in glutamic acid decarboxylase 2 (GAD2)-positive GABAergic neurons (Figure S3). To record neural activity following ME stimulation, we again inserted a stereotrode attached to the biphasic ME stimulator described above and imaged local GCaMP3 fluorescence increases using a 60× water immersion lens (Figures S3A–S3C; STAR Methods). Due to the background fluorescence and scattering, we observed only overall fluorescence changes in the field of view (300 × 300 µm), which contains up to 100 GCaMP3-positive neurons that could contribute to the observed signal (Keller et al., 2018). We chose neural stimulation parameters of 100 biphasic pulses at 200 Hz ,with each phase lasting 175 µs. When the magnetic field was on, we observed a corresponding increase in fluorescence in the neocortical layer 5 (n = 23 recordings obtained in 2 brain slices), which was consistent with stimulus-evoked calcium increases in local neurons. Following bath application of tetrodotoxin (TTX; 500 nM), fluorescence increases were completely blocked in n = 9 recordings, confirming that ME-evoked calcium increases were dependent on APs. Positive results in both slices analyzed were sufficient to qualitatively confirm that neurons were reliably activated by our ME stimulator.

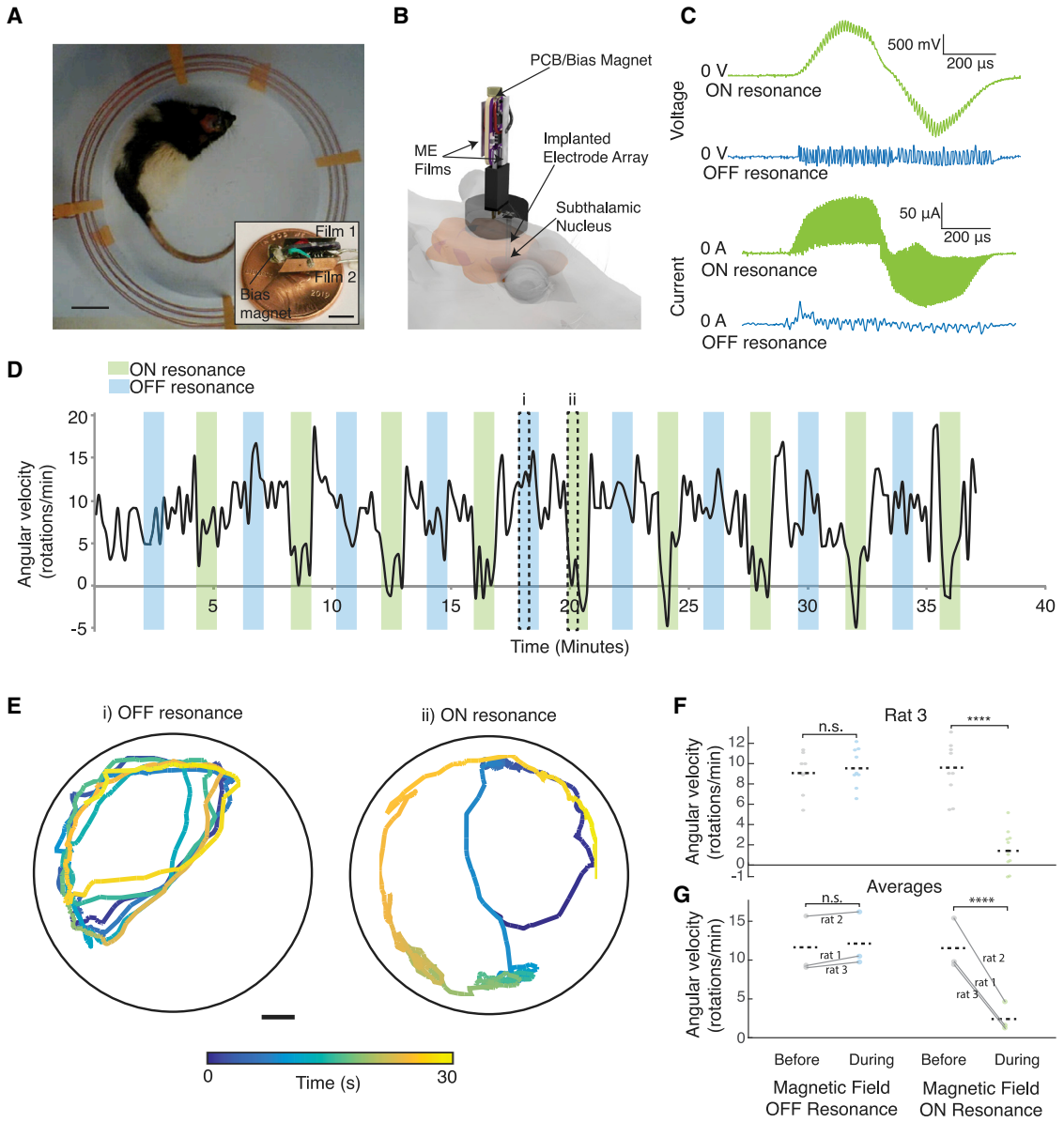

Figure 4. Effective DBS in a Freely Moving Rat using a Wireless ME Stimulator

(A) Experimental setup showing rat in a circular enclosure wrapped with a coil; scale bar, 5 cm. Inset shows a biphasic ME stimulator on a one-cent coin; scale bar, 5 mm.

(B) Schematic of the biphasic ME stimulator attached to the electrode array implanted into the STN.

(C) Measured voltage generated by the ME device and the current applied to the brain ON resonance (green) and OFF resonance (blue).

(D) Angular velocity of the hemi-parkinsonian rat over a 40-min trial with intervals of resonant and non-resonant stimulation, showing reduced rotations when the stimulator is activated on resonance.

(E) Typical trajectories show the location of the animal's head over two 30-s intervals denoted in (C); scale bar, 5 cm.

(F) Average angular velocity of the rat during the 30 s before stimulation and the first 30 s of stimulation for each interval during the 40-min experiment (****$p = 4 \times 10^{-7}$; n.s., not significant; $p = 0.70$, paired t test).

(G) Average angular velocities for n = 3 rats shows repeatable results across animals (****$p = 2.8 \times 10^{-18}$; $p = 0.11$, paired t test). See also Figure S4 and Videos S2 and S3.

ME Neural Stimulation in Freely Moving Rats Provides Therapeutic Benefit

A major advantage of our ME stimulators is that remote activation enables experiments with freely behaving animals. As a proof-of-principle, we adapted our biphasic stimulator for DBS in freely moving rats (Figure 4). To test ME stimulator efficacy, we used a previously reported protocol to test DBS in hemi-parkinsonian rats (Summerson et al., 2014). In these

experiments, rats are injected with 6-OHDA (oxydopamine) in the left medial forebrain bundle (MFB) to create a unilateral lesion of the substantia nigra pars compacta (SNc). The animals are then placed in a 30-cm-diameter circular enclosure. Following a dose of methamphetamine, the hemi-parkinsonian rats have been shown to rotate ipsilateral to the injection (e.g., left for injection into the left MFB). During these rotations, the rat primarily moves using its contralateral (right) forepaw, rarely placing the ipsilateral (left) forepaw onto the ground. When a biphasic stimulus is applied at 200 Hz in the sub-thalamic nucleus (STN) by using a tethered electrode array stimulator, rats typically stop turning to the left and exhibit more normal behavior, such as moving with both forepaws, maintaining a steady orientation, or turning to the contralateral side (So et al., 2017).

To create a wireless, biphasic ME stimulator for freely moving animals, we added a small permanent magnet (<0.25 g) to the ME stimulator to generate a bias field as the animal moved and wrapped the behavioral chamber with wire to create a solenoid for the alternating magnetic field (Figures 4A and S4). This 0.5-g ME stimulator was then connected to a commercial electrode array (Microprobes) implanted in the STN (Figure 4B; see STAR Methods). We ensured that the stimulation voltage and current were within the safe and therapeutic range by measuring the output of the ME stimulator connected to an equivalent circuit model of the brain (Figure 4C; see STAR Methods). Specifically, we observed peak voltages of approximately ±1.5 V and peak currents of approximately ±100 μA for 400 μs at approximately a 50% duty cycle (200 μs of overall current per phase), which is within the effective stimulation range reported for conventional wired stimulators (Summerson et al., 2014). When we tune the magnetic field frequency off resonance we observe almost no generated voltage or current (Figure 4C).

We then tested our wireless biphasic ME stimulator mounted to the head of a rat and found that ME stimulation showed efficacy comparable to previously reported wired DBS stimulators (Figure 4). With a magnetic field applied at resonance, we found that 1-min periods of 200-Hz biphasic pulses resulted in a significant decrease in the animal's rotation rate (Figure 4D, green intervals). This decreased rotation was not observed when the magnetic stimulus frequency was tuned off resonance (Figure 4D, blue intervals). Plots of the head trajectories show that the pathological ipsilateral rotations observed during off-resonant magnetic field stimulation are not present when the ME stimulator is active during resonant magnetic field stimulation where the rotations are either not present or contralateral, as expected for successful stimulation (Figure 4E; Videos S2 and S3; STAR Methods). When averaged over all trials, the average rotation rate during the first half of stimulation fell to a statistically significant 1.4 rotations per minute (rpm), compared to 9.4 rpm in the absence of stimulation, or 10.6 rpm during off-resonant stimulation (paired t test; Figure 4F). We further demonstrated the repeatability of these results by repeating this stimulation protocol on two other rats and found similar results (Figures 4G and S4). A power analysis based on our proof-of-concept data suggests that future neuroscience experiments using this technology for hypothesis testing would require larger cohorts of approximately 6 rats (Figure S4C).

Millimeter-Sized ME Devices Enable Fully Implanted Biphasic Stimulation in Freely Behaving Rodents

By miniaturizing the components of our stimulator, we created a fully implanted version of our biphasic stimulators (Figure 5). This biphasic device is composed of two millimeter-sized ME films (4.3 mm × 2 mm and 5.4 mm × 2 mm in area) connected with circuit elements described previously (Figure 5B) and wired to a stereotrode. We packaged the device using a 3D-printed plastic shell coated in epoxy to protect the films and circuit from the surrounding biological environment (Figure S5B). This miniature design enabled the films and circuitry to be placed on the skull of the rat with the skin sutured up over the implant (Figures 5A and 5E), which could help prevent issues arising from percutaneous leads.

We performed a place preference experiment to demonstrate that this fully implanted device effectively stimulates neural activity in a freely moving rodent. Because this experiment requires greater stimulation currents than the DBS experiment, we replaced the PVDF piezoelectric layer with PZT (Figure 5C). We then implanted the device connected to a stereotrode surgically placed in the MFB, which is part of the reward pathway commonly used to drive behavior (Olds and Milner 1954). One to 3 days following surgery, we placed each rat (n = 3) on a linear track with two custom-designed double resonant coils at either end of the track. For each experiment, the coil at one end for the track was ON resonance for both of the implanted films and the coil at the other end of the track was OFF resonance. To test for any confounding effects of the magnetic field, we ensured that each coil produced the same field strength of 1.5 mT (Figures 5D and S5A). When the rat's head was inside the ON resonant coil, the device was activated, stimulating dopaminergic neurons in the MFB and inducing a location preference for that coil (Figure 5D; Video S4). We quantified this effect by analyzing the amount of time the rat spent in the ON resonant coil compared to the OFF resonant coil in six 10-min trials/rat. To demonstrate that this effect was due to the ME device, we performed three trials and then switched which coil was on resonance for another three trials. As expected, we found that the place preference switched to match which coil was on resonance with our implant (Figures 5F, 5G, S5C, and S5D). In each case, we see a significant preference for the ON resonant coil, which confirmed that this fully implanted biphasic device is an effective neural stimulator. We again performed a power analysis based on these data to determine the approximate cohort size that would be needed for hypothesis testing using this approach (Figure S5E).

DISCUSSION

The advantages of ME materials extend beyond these proof-of-principle demonstrations. ME materials have the potential to enable miniature neural stimulators that can be implanted deep in the brain of large animals or humans and activated externally with an electromagnet. Additional miniaturization from the rice-sized device shown here is not expected to reduce the film voltage, suggesting that even smaller films could serve as effective stimulators. In the future, the rectifying diode and/or LED

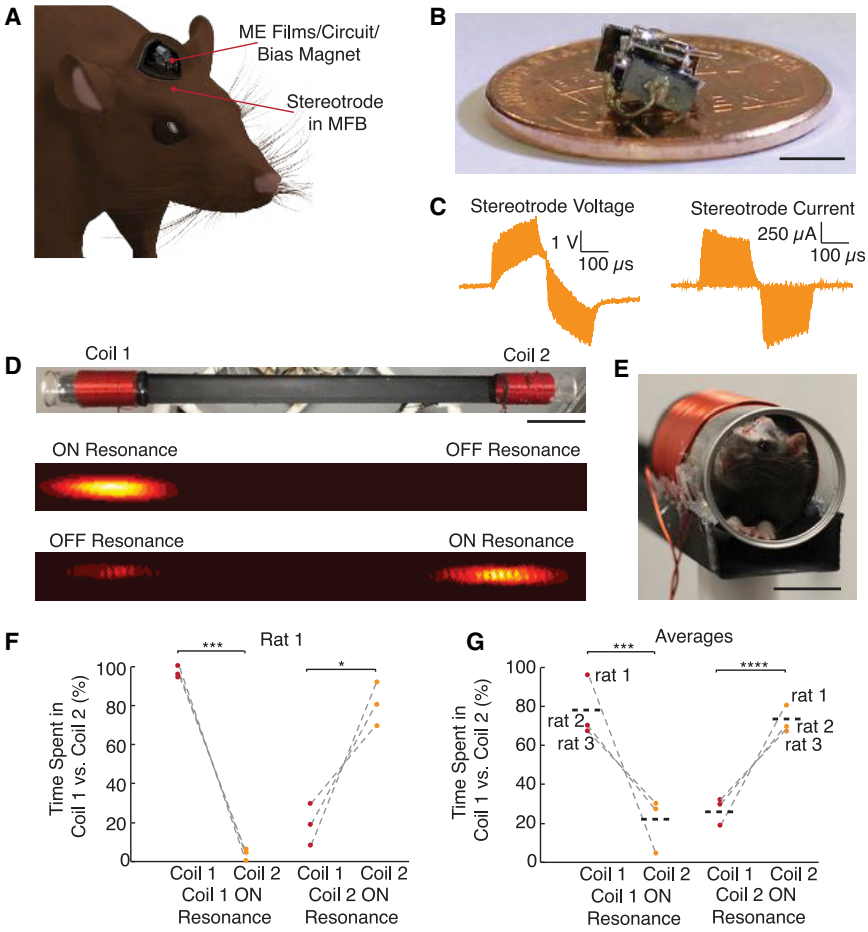

Figure 5. Fully Implanted ME Device Stimulates Place Preference in Freely Moving Rats

(A) Schematic of the device implanted under the skin of a rat with stereotrode implanted into the MFB.

(B) Inner circuit and films used in the implant; scale bar, 5 mm.

(C) Representative voltage and current waveforms used for stimulation.

(D) Experimental setup of the linear track and representative heatmaps for two individual trials showing a preference for the ON resonance coil showing we could change the preference by altering the frequencies in each coil; scale bar, 10 cm.

(E) Side view of the setup showing a rat in the coil with the skin sutured over the implant; scale bar, 3 cm.

(F) Preference results from one rat over six trials (***$p = 9 \times 10^{-4}$, *$p = 0.038$, paired t test).

(G) Average results for n = 3 rats show repeatability across animals (***$p = 2.7 \times 10^{-4}$, ****$p = 3.6 \times 10^{-5}$, paired t test). See also Figure S5 and Video S4.

could be fabricated directly onto the ME film by using lithography techniques, enabling miniature materials-based ME stimulators.

External ME stimulators, such as the one described in the *in vivo* rotation experiment, could have an immediate effect on the study of DBS therapies using rodent disease models. Because the ME stimulator is compatible with commercial implanted electrodes and the magnetic stimulators can be adapted to a number of standard behavioral experiments or animal enclosures, our ME stimulators could readily replace the wired DBS stimulators currently in use. As a result, new experiments can be developed to probe the effects of chronic and continuous DBS or DBS in social contexts in which wired DBS stimulators would be impracticable.

Fully implanted ME stimulators have further advantages of avoiding routes for infection and allow for even more freedom of movement and social interaction between animals. Devices like these could also be adapted to target different brain areas or peripheral nerves by using commercially available or custom designed electrodes.

Our preliminary lifetime testing showed good performance under physiological conditions, but more work is needed to develop packaging solutions for chronic *in vivo* applications. Specifically, we found that these miniaturized ME films, when encapsulated with polyimide, maintained their functionality during a 14-day soak test in 37°C saline (Figure S6E). Additionally, when we placed the coated films into an agarose gel that closely matches the mechanical properties of brain tissue, we found only a 20% decrease in voltage as a result of this mechanical dampening (Figure S6F). Because films can produce 10–30 V, we expect these films to function under biological conditions. To avoid dampening, one could design packaging solutions that reduce the mechanical coupling between the film and the tissue. Future testing, including immunohistochemistry, will be needed to assess the foreign body response and develop packaging that limits this response and is stable for chronic use.

For applications that require chronic high-frequency stimulation, it will be important to measure the internal device losses due to heat and pressure waves and how this could affect tissue. As a preliminary experiment, we measured the temperature of the film following 5 min of pulsed activation (ME film = 6 $V_{peak\text{-}peak}$ and 20% duty cycle at 100 Hz) and observed no increase in the film temperature (Figures S6C and S6D). Should pressure waves pose a hazard, one could develop packaging solutions that minimized the mechanical coupling between the film and the tissue.

The overall volume of the fully implanted stimulator, although small compared to conventional stimulators, remains relatively large compared to other recent implanted technologies (Table 1). However, the size of the ME power source is small (2–4 mm^3; Table 1), and the bulk of the implant is packaging, bias magnet, and off-the-shelf circuit elements. Further miniaturization is possible with improved layouts and packaging as well as with custom miniature integrated circuits, which, together with further deceases in the ME film size, could lead to sub-millimeter-sized implantable devices. A potential challenge with future free-floating devices for clinical applications is that they could migrate

over time from the target tissue. Future work should address this and explore methods to anchor or tether the devices by using biocompatible adhesives (Mahdavi et al., 2008) or mechanical anchors like nerve cuffs (Piech et al., 2020).

The arena size used in the rotation experiment is comparable to other studies using RF-powered devices, and future work should focus on exploring larger arenas and the associated engineering challenges. Our calculations suggest that we can reconfigure the drive coils for a number of behavioral experiments by placing coils beneath the floor of an animal enclosure. Simulations and measurements show that at 4–5 cm above a drive coil, ME films generate sufficient voltage for some low levels of stimulation (Figures S6A and S6B). This distance could be further improved by optimizing the geometry of the coils or increasing the power of the magnetic field.

The performance and application space for ME stimulators can be greatly expanded by adding application-specific integrated circuits (ASICs). With these circuits, one could create biphasic stimulation by using a single ME film or generate wirelessly programmable stimulation at various specified voltage levels (Yu et al., 2020). Additionally, one can imagine networks of devices that can be individually addressed using wireless network protocols implemented in the ASICs. This ability to ensure safe and effective stimulation with integrated circuits will likely be required for clinical translation of this technology.

We also foresee applications for ME materials as a wireless power technology for more complex implantable bioelectronic devices. For example, the demonstrated ability of ME films to power LEDs implies that ME materials could power implantable optogenetic stimulators, small integrated circuits for physiological monitoring, or transmit data out for closed-loop bioelectronic devices. For wearable technologies, it is also necessary to further miniaturize magnetic field generators so that they can be battery powered and comfortably worn.

With the benefits of ME-based bioelectronics also come limitations. The need for magnetic materials may limit the magnetic imaging compatibility of some devices. Compared to ultrasound and RF wireless power that rely on propagating waves, our ME devices are powered by near-field magnetic fields. As a result, the depth that we can effectively power ME devices depends on the size of the transmitter. On other hand, the magnetic fields used here show negligible absorption by the tissue, allowing us to increase the power in the transmitter and remain well below the safety limits. Together, these considerations provide design tradeoffs to considder when developing a system for miniature bioelectronic implants, where the constraints on the size of the transmitter, need to transmit through air, and total power needed at the device may lead one to choose one wireless power solution over another. Additionally, bidirectional communication based on ME effects may be difficult because the magnetic fields do not radiate like ultrasound or EM waves.

ME materials have the potential to fill a key need for wireless power delivery to miniature neural stimulators and other bioelectronic devices for which the major challenge is transferring energy over distances of several centimeters without heating the tissue or suffering loss at interfaces between tissue, bone, and air.

STAR★METHODS

Detailed methods are provided in the online version of this paper and include the following:

- KEY RESOURCES TABLE
- RESOURCE AVAILABILITY
  - Lead Contact
  - Materials Availability
  - Data and Code Availability
- EXPERIMENTAL MODEL AND SUBJECT DETAILS
  - Cell Lines
  - Animals
- METHOD DETAILS
  - Film Fabrication
  - Bench Top Electrolysis Tests
  - Alternating Magnetic Field Generation (Figure S1)
  - Resonant Coil Design
  - *In Vitro* HEK Experiments
  - Skull Phantom Demonstration
  - Two film biphasic circuit design
  - Electrophysiology
  - GCaMP Imaging
  - Rat Surgical Procedures
  - Hemi-Parkinsonian Experiments
  - Rodent Tracking
  - Place Preference Implant Design
  - Place Preference Experiments
- QUANTIFICATION AND STATISTICAL ANALYSIS

SUPPLEMENTAL INFORMATION

Supplemental Information can be found online at https://doi.org/10.1016/j.neuron.2020.05.019.

ACKNOWLEDGMENTS

The authors thank Michael Beauchamp for useful discussions and our attending veterinarian at Rice University, Dr. Elysse Orchard, for help with the surgical procedures. This research was supported by the National Institute of Health (United States) through the NIH HEAL Initiative under award number 1U18EB029353-01, and NIH award number R21EY028397A. This material is based upon work supported by the National Science Foundation (United States) under Grant No. CBET-1351692, IGERT 1250104 (A.S. and E.L.), and NSF GRFP 1842494 (J.C.C.).

AUTHOR CONTRIBUTIONS

Conceptualization, A.S. and J.T.R.; Methodology, A.S., S.D., M.B., C.K., and J.T.R.; Software, B.A., S.D., and A.K.F.; Investigation, A.S., S.D., E.L., Z.C., J.C.C., N.V., A.K.F., and J.O.; Resources, M.B., C.K., and J.T.R.; Writing–Original Draft, A.S. and J.T.R.; Writing–Review and Editing, A.S., J.C.C., and J.T.R.; Funding Acquisition, C.K. and J.T.R.

DECLARATION OF INTERESTS

This work relates to patent PCT/US2020/026688.

Received: November 19, 2018
Revised: March 9, 2020
Accepted: May 12, 2020
Published: June 8, 2020

REFERENCES

Agmon, A., and Connors, B.W. (1991). Thalamocortical responses of mouse somatosensory (barrel) cortex in vitro. Neuroscience *41*, 365–379.

Agrawal, D.R., Tanabe, Y., Weng, D., Ma, A., Hsu, S., Liao, S.Y., Zhen, Z., Zhu, Z.Y., Sun, C., Dong, Z., et al. (2017). Conformal phased surfaces for wireless powering of bioelectronic microdevices. Nat. Biomed. Eng. *1*, 1–16.

Alonso, P., Cuadras, D., Gabriëls, L., Denys, D., Goodman, W., Greenberg, B.D., Jimenez-Ponce, F., Kuhn, J., Lenartz, D., Mallet, L., et al. (2015). Deep brain stimulation for obsessive-compulsive disorder: A meta-analysis of treatment outcome and predictors of response. PLoS One *10*, e0133591.

Baizabal-Carvallo, J.F., and Alonso-Juarez, M. (2016). Low-frequency deep brain stimulation for movement disorders. Parkinsonism Relat. Disord. *31*, 14–22.

Ben Amar, A., Kouki, A.B., and Cao, H. (2015). Power approaches for implantable medical devices. Sensors (Basel) *15*, 28889–28914.

Bewernick, B.H., Hurlemann, R., Matusch, A., Kayser, S., Grubert, C., Hadrysiewicz, B., Axmacher, N., Lemke, M., Cooper-Mahkorn, D., Cohen, M.X., et al. (2010). Nucleus accumbens deep brain stimulation decreases ratings of depression and anxiety in treatment-resistant depression. Biol. Psychiatry *67*, 110–116.

Biran, R., Martin, D.C., and Tresco, P.A. (2007). The brain tissue response to implanted silicon microelectrode arrays is increased when the device is tethered to the skull. J. Biomed. Mater. Res. A *82*, 169–178.

Bottomley, P.A., and Andrew, E.R. (1978). RF magnetic field penetration, phase shift and power dissipation in biological tissue: implications for NMR imaging. Phys. Med. Biol. *23*, 630–643.

Carrey, J., Mehdaoui, B., and Respaud, M. (2011). Simple models for dynamic hysteresis loop calculations of magnetic single-domain nanoparticles: Application to magnetic hyperthermia optimization. J. Appl. Phys. *109*, 83921.

Chen, R., Romero, G., Christiansen, M.G., Mohr, A., and Anikeeva, P. (2015). Wireless magnetothermal deep brain stimulation. Science *347*, 1477–1480.

de Hemptinne, C., Swann, N.C., Ostrem, J.L., Ryapolova-Webb, E.S., San Luciano, M., Galifianakis, N.B., and Starr, P.A. (2015). Therapeutic deep brain stimulation reduces cortical phase-amplitude coupling in Parkinson's disease. Nat. Neurosci. *18*, 779–786.

Fotopoulou, K., and Flynn, B.W. (2011). Wireless Power Transfer in Loosely Coupled Links: Coil Misalignment Model. IEEE Trans. Magn. *47*, 416–430.

Freeman, D.K., O'Brien, J.M., Kumar, P., Daniels, B., Irion, R.A., Shraytah, L., Ingersoll, B.K., Magyar, A.P., Czarnecki, A., Wheeler, J., et al. (2017). A sub-millimeter, inductively powered neural stimulator. Front. Neurosci. *11*, 659.

Guduru, R., Liang, P., Hong, J., Rodzinski, A., Hadjikhani, A., Horstmyer, J., Levister, E., and Khizroev, S. (2015). Magnetoelectric 'spin' on stimulating the brain. Nanomedicine (Lond.) *10*, 2051–2061.

Hargreaves, D.G., Drew, S.J., and Eckersley, R. (2004). Kirschner wire pin tract infection rates: a randomized controlled trial between percutaneous and buried wires. J. Hand Surg. Br. *29*, 374–376.

Ho, J.S., Tanabe, Y., Iyer, S.M., Christensen, A.J., Grosenick, L., Deisseroth, K., Delp, S.L., and Poon, A.S.Y. (2015). Self-Tracking Energy Transfer for Neural Stimulation in Untethered Mice. Phys. Rev. Appl. *4*, 024001.

IEEE. (2006). IEEE Standard for Safety Levels with Respect to Human Exposure to Radio Frequency Electromagnetic Fields, 3 kHz to 300 GHz. EEE, 1–238, Std C95.1-2005.

Jin, L., Han, Z., Platisa, J., Wooltorton, J.R., Cohen, L.B., and Pieribone, V.A. (2012). Single action potentials and subthreshold electrical events imaged in neurons with a fluorescent protein voltage probe. Neuron *75*, 779–785.

Johnson, B.C., Shen, K., Piech, D., Ghanbari, M.M., Liu, K.Y., Neely, R., Carmena, J.M., Maharbiz, M.M., and Muller, R. (2018). StimDust : A 6.5mm3, Wireless Ultrasonic Peripheral Nerve Stimulator with 82% Peak Chip Efficiency. 2018 IEEE Custom Integrated Circuits Conference.

Keller, D., Erö, C., and Markram, H. (2018). Cell Densities in the Mouse Brain: A Systematic Review. Front. Neuroanat. *12*, 83.

Kesar, T.M., Perumal, R., Jancosko, A., Reisman, D.S., Rudolph, K.S., Higginson, J.S., and Binder-Macleod, S.A. (2010). Novel patterns of functional electrical stimulation have an immediate effect on dorsiflexor muscle function during gait for people poststroke. Phys. Ther. *90*, 55–66.

Kulkarni, A., Meurisch, K., Teliban, I., Jahns, R., Strunskus, T., Piorra, A., Knöchel, R., and Faupel, F. (2014). Giant magnetoelectric effect at low frequencies in polymer-based thin film composites. Appl. Phys. Lett. *104*, 022904.

Maeng, L.Y., Murillo, M.F., Mu, M., Lo, M.C., de la Rosa, M., O'Brien, J.M., Freeman, D.K., and Widge, A.S. (2019). Behavioral validation of a wireless low-power neurostimulation technology in a conditioned place preference task. J. Neural Eng. *16*, 026022.

Mahdavi, A., Ferreira, L., Sundback, C., Nichol, J.W., Chan, E.P., Carter, D.J., Bettinger, C.J., Patanavanich, S., Chignozha, L., Ben-Joseph, E., et al. (2008). A biodegradable and biocompatible gecko-inspired tissue adhesive. Proc. Natl. Acad. Sci. USA *105*, 2307–2312.

Markwardt, N.T., Stokol, J., and Rennaker, R.L., II (2013). Sub-meninges implantation reduces immune response to neural implants. J. Neurosci. Methods *214*, 119–125.

Mathis, A., Mamidanna, P., Cury, K.M., Abe, T., Murthy, V.N., Mathis, M.W., and Bethge, M. (2018). DeepLabCut: markerless pose estimation of user-defined body parts with deep learning. Nat. Neurosci. *21*, 1281–1289.

Merrill, D.R., Bikson, M., and Jefferys, J.G.R. (2005). Electrical stimulation of excitable tissue: design of efficacious and safe protocols. J. Neurosci. Methods *141*, 171–198.

Montgomery, K.L., Yeh, A.J., Ho, J.S., Tsao, V., Mohan Iyer, S., Grosenick, L., Ferenczi, E.A., Tanabe, Y., Deisseroth, K., Delp, S.L., and Poon, A.S. (2015). Wirelessly powered, fully internal optogenetics for brain, spinal and peripheral circuits in mice. Nat. Methods *12*, 969–974.

Mulpuru, S.K., Madhavan, M., McLeod, C.J., Cha, Y.M., and Friedman, P.A. (2017). Cardiac Pacemakers: Function, Troubleshooting, and Management: Part 1 of a 2-Part Series. J. Am. Coll. Cardiol. *69*, 189–210.

Munshi, R., Qadri, S.M., Zhang, Q., Castellanos Rubio, I., Del Pino, P., and Pralle, A. (2017). Magnetothermal genetic deep brain stimulation of motor behaviors in awake, freely moving mice. eLife *6*, 1–26.

Nan, T., Lin, H., Gao, Y., Matyushov, A., Yu, G., Chen, H., Sun, N., Wei, S., Wang, Z., Li, M., et al. (2017). Acoustically actuated ultra-compact NEMS magnetoelectric antennas. Nat. Commun. *8*, 296.

Nurmikko, A.V. (2018). Approaches to large scale neural recording by chronic implants for mobile BCIs. 2018 6th International Conference on Brain-Computer Interface, 1–2.

O'Handley, R.C., et al. (2008). Improved Wireless, Transcutaneous Power Transmission for *In Vivo* Applications. IEEE Sens. J. *8*, 57–62.

Olds, J., and Milner, P. (1954). Positive reinforcement produced by electrical stimulation of septal area and other regions of rat brain. J. Comp. Physiol. Psychol. *47*, 419–427.

Parastarfeizabadi, M., and Kouzani, A.Z. (2017). Advances in closed-loop deep brain stimulation devices. J. Neuroeng. Rehabil. *14*, 79.

Park, J., Werley, C.A., Venkatachalam, V., Kralj, J.M., Dib-Hajj, S.D., Waxman, S.G., and Cohen, A.E. (2013). Screening fluorescent voltage indicators with spontaneously spiking HEK cells. PLoS One *8*, e85221.

Park, S.I., Shin, G., McCall, J.G., Al-Hasani, R., Norris, A., Xia, L., Brenner, D.S., Noh, K.N., Bang, S.Y., Bhatti, D.L., et al. (2016). Stretchable multichannel antennas in soft wireless optoelectronic implants for optogenetics. Proc. Natl. Acad. Sci. USA *113*, E8169–E8177.

Piech, D.K., Johnson, B.C., Shen, K., Ghanbari, M.M., Li, K.Y., Neely, R.M., Kay, J.E., Carmena, J.M., Maharbiz, M.M., and Muller, R. (2020). A wireless millimetre-scale implantable neural stimulator with ultrasonically powered bidirectional communication. Nat. Biomed. Eng. *4*, 207–222.

Pinnell, R.C., Pereira de Vasconcelos, A., Cassel, J.C., and Hofmann, U.G. (2018). A Miniaturized, Programmable Deep-Brain Stimulator for Group-Housing and Water Maze Use. Front. Neurosci. *12*, 231.

Ribeiro, C., Correia, V., Martins, P., Gama, F.M., and Lanceros-Mendez, S. (2016). Proving the suitability of magnetoelectric stimuli for tissue engineering applications. Colloids Surf. B Biointerfaces *140*, 430–436.

Sahin, M., and Pikov, V. (2011). Wireless microstimulators for neural prosthetics. Crit. Rev. Biomed. Eng. *39*, 63–77.

Schabrun, S.M., Jones, E., Elgueta Cancino, E.L., and Hodges, P.W. (2014). Targeting chronic recurrent low back pain from the top-down and the bottom-up: a combined transcranial direct current stimulation and peripheral electrical stimulation intervention. Brain Stimul. *7*, 451–459.

Seo, D., Neely, R.M., Shen, K., Singhal, U., Alon, E., Rabaey, J.M., Carmena, J.M., and Maharbiz, M.M. (2016). Wireless Recording in the Peripheral Nervous System with Ultrasonic Neural Dust. Neuron *91*, 529–539.

Shin, G., Gomez, A.M., Al-Hasani, R., Jeong, Y.R., Kim, J., Xie, Z., Banks, A., Lee, S.M., Han, S.Y., Yoo, C.J., et al. (2017). Flexible Near-Field Wireless Optoelectronics as Subdermal Implants for Broad Applications in Optogenetics. Neuron *93*, 509–521.e3.

So, R.Q., McConnell, G.C., and Grill, W.M. (2017). Frequency-dependent, transient effects of subthalamic nucleus deep brain stimulation on methamphetamine-induced circling and neuronal activity in the hemiparkinsonian rat. Behav. Brain Res. *320*, 119–127.

Summerson, S.R., Aazhang, B., and Kemere, C.T. (2014). Characterizing motor and cognitive effects associated with deep brain stimulation in the GPi of hemi-Parkinsonian rats. IEEE Trans. Neural Syst. Rehabil. Eng. *22*, 1218–1227.

Sun, Y., Greet, D., Burkland, M., John, M., Razavi, M., and Babakhani, A. (2017). Wirelessly Powered Implantable Pacemaker with On-Chip Antenna (IEEE), pp. 1242–1244.

Theodore, W.H., and Fisher, R.S. (2004). Brain stimulation for epilepsy. Lancet Neurol. *3*, 111–118.

Ting, J.T., Daigle, T.L., Chen, Q., and Feng, G. (2014). Acute brain slice methods for adult and aging animals: application of targeted patch clamp analysis and optogenetics. Methods Mol. Biol. *1183*, 221–242.

Wan, C., and Bowen, C.R. (2017). Multiscale-structuring of polyvinylidene fluoride for energy harvesting: the impact of molecular-, micro- and macro-structure. J. Mater. Chem. A *5*, 3091–3128.

Yu, Z., Chen, J.C., Avants, B.W., He, Y., Singer, A., Robinson, J.T., and Yang, K. (2020). An 8.2mm^3 Implantable Neurostimulator with Magnetoelectric Power and Data Transfer. 2020 IEEE International Solid-State Circuits Conference - (ISSCC), 510–512.

Yue, K., Guduru, R., Hong, J., Liang, P., Nair, M., and Khizroev, S. (2012). Magneto-electric nano-particles for non-invasive brain stimulation. PLoS One *7*, e44040.

Zhai, J., et al. (2006). Giant magnetoelectric effect in Metglas/polyvinylidene-fluoride laminates. Appl. Phys. Lett. *89*, 8–11.

STAR★METHODS

KEY RESOURCES TABLE

REAGENT or RESOURCE	SOURCE	IDENTIFIER
Experimental Models: Cell Lines		
Spiking HEK Cells	Park et al., 2013	N/A
Experimental Models: Organisms/Strains		
Rat: Long Evans	Charles River	RRID:RGD_2308852
Mouse: C57BL6/J	The Jackson Laboratory	# 000664
Mouse: GAD2-Cre	The Jackson Laboratory	# 10802
Mouse: flox-GCaMP3	The Jackson Laboratory	# 14538
Recombinant DNA		
Plasmid: ArcLight-A242	Addgene	Plasmid #36857
Software and Algorithms		
Magnetic Field Driver Code	Robinson Lab	https://github.com/RobinsonLab-Rice/MagElecCoilDriver
MATLAB	Mathworks, MA	https://www.mathworks.com/downloads/
Python	Python Software Foundation	https://www.python.org/downloads/
COMSOL Multiphysics	Comsol, Inc.	https://www.comsol.com/products
Other		
Metglas	Metglas, Inc.	2605sa1
PVDF	Precision Acoustics	https://www.acoustics.co.uk/product/pvdf/
PZT	Piezo Systems	T105-A4NO-2929
Electrode Array	Microprobes	Custom Order
Stereotrode	Microprobes	Custom Order

RESOURCE AVAILABILITY

Lead Contact

Further information and requests for resources and reagents should be directed to the Lead Contact, Jacob T. Robinson (jtrobinson@rice.edu).

Materials Availability

This study did not generate new unique reagents.

Data and Code Availability

The arduino teensy code used to drive the magnetic fields can be found at: https://github.com/RobinsonLab-Rice/MagElecCoilDriver

EXPERIMENTAL MODEL AND SUBJECT DETAILS

Cell Lines

HEK cells expressing sodium channel $Na_{1.3}$ and potassium channel $K_{2.1}$ were obtained from the lab of Dr. Adam Cohen (Harvard). Cells were cultured and maintained at 37°C in cell culture media (DMEM/f12 with strep, pen, geneticin, and puromycin)

Animals

Brain slice experiments

All experiments were performed in accordance with NIH guidelines and approved by the University of Texas Health Science Center at Houston (UTHealth) animal welfare committee. For electrophysiology, we used 16-day-old male C57BL6/J mice (JAX #000664). For

GCaMP imaging we used 40-day-old male GAD2-GCaMP3 mice, generated by crossing GAD2-Cre (JAX # 10802) with flox-GCaMP3 (JAX # 14538) animals.

In vivo *experiments*

All experiments were approved by the Rice University Institutional Animal Care and Use Committee's guidelines and adhered to the National Institute of Health guidelines. Six adult male Long-Evans rats aged 4-7 months and weighing 500-800 g from Charles River Laboratories were used for this study. Rats were housed in pairs prior to surgery and randomly chosen for implantation. Post-implantation rats were individually housed. At all times animals were kept on a 12 hour light-dark cycle.

METHOD DETAILS

Film Fabrication

To fabricate ME films, we used Metglas SA1 alloy (Metglas Inc) for the magnetostrictive layer and polyvinylidenefluoride "PVDF" (precision acoustics) or lead Zirconate titanate "PZT" (Piezo Systems) for the piezoelectric layer. The d_{31} coefficient is 22 pC/N for PVDF (Precision Acoustics) and 320 pC/N for PZT (Piezo Systems) . The PVDF films used for these experiments were pre-stretched and poled by the manufacturer. The two layers were bonded together using an epoxy capable of transferring the mechanical stress between the two layers (Hardman double bubble red epoxy). Prior to bonding the two layers together, we sputtered a thin layer of Platinum (< 100 nm) as a top electrode on the PVDF. The PZT films are manufactured with a nickel top electrode. Both the Metglas and PVDF were plasma cleaned using O_2 plasma for five minutes before epoxying. After the epoxy set, the films were cut into the desired rectangular shape using scissors, taking care to cut the long axis of the film along the stretching direction of the PVDF. We then attached wires using conductive epoxy to either side of the films in order to measure the electrical capabilities of the film. We found that attaching wires in the center dramatically increased the resonant voltage. However for convenience, the wires were attached near the ends of the films during the *in vitro* experiments. In many cases we also attached additional electronic components such as diodes or LEDs to the wires attached to the films as noted in the appropriate sections in the main text. Finally the devices were coated in 5-10 μm of parylene-C (Labcoater 2). Initially this coating was used to electrically insulate and protect the devices during *in vitro* experiments, but we also found that the encapsulation increases the resonant voltage, which could be due to increased mechanical coupling from the encapsulation.

Bench Top Electrolysis Tests

The stimulator shown in Figure 4A was wired to a stereotrode immersed in saline under a microscope in order to observe the formation of bubbles from electrolysis at the tips. During monophasic stimulation we used only one resonant frequency and during biphasic stimulation we used two frequencies as demonstrated above. In each case the pulse time was a 400 μs/phase. We determined the limit of stimulation time as when the first bubble began to appear at the tips of the electrode and repeated each data point 4 times.

Alternating Magnetic Field Generation (Figure S1)

Each magnetic field generator consists of two major components, 1) Magnetic coils used for the alternating magnetic field (described in the main text and optimized for each experiment) and 2) Electronic drivers to control voltage and timing of the alternating current in the coils (the same for all experiments). The addition of a bias field allows us to generate therapeutic voltage levels while applying a small (few mT) alternating magnetic field around this central bias point using an electromagnetic coil and custom control circuitry that specifies the frequency and timing of the alternating magnetic field (Figures S1E–S1H).

To maintain simplicity, efficiency, and low cost the coils were driven with full H-Bridge style switching circuits. The drivers are designed to deliver high currents to the drive coils in the form of bi-phasic pulse trains. This reduces the cost and complexity of the driver itself, as well as the power supply and control circuitry when compared to arbitrary function generators. The design also has potential for improved operational efficiency through impedance matching with the drive coils. Furthermore, it is also possible to regulate power delivered to the drive coils on the fly by adjusting the duty cycle of the current pulses, allowing power being delivered to the ME film to be easily controlled digitally while maintaining the resonant carrier frequency. The output carrier and pulse frequencies of the magnetic field are generated using a TeensyLC board and custom Arduino code to generate the specific pulse timings to deliver controlled ME stimulation (Figures S1E–S1H).

These coils and drivers can be combined in different ways to generate the appropriate field for a given experiment. For example, the setup used to generate the alternating field in the *in vivo* rotation experiments consisted of four sets of coils each with five turns powered by one driver with all four drivers synced to the same output signal. In this way we can generate sufficient power to generate a mT-scale magnetic fields over the whole behavioral area (Figures S4A and S4B).

Resonant Coil Design

In order to generate sufficient field strengths of > 1mT at the resonant frequencies for the miniature devices (300-400 kHz) we developed a custom resonant coil system as shown in Figure S5. This system had two separate resonant frequencies to be able to selectively active each film on the miniature device. The first higher resonance is determined by a single capacitor C_1 in series with the

behavioral coil while the self-resonance from a second inductor acts as a low pass filter to prevent a second capacitor C_2 from affecting the system. The second lower series resonance is determined from adding C_1 and C_2 in parallel as the inductor no longer filters out the lower resonant frequency.

In Vitro HEK Experiments

For experiments performed on coverslips, HEK cells expressing sodium channel $Na_{1.3}$ and potassium channel $K_{2.1}$ were grown on 12 mm poly-l-lysine coated coverslips to approximately 30% confluency. The cells were then transfected with the genetically encoded voltage indicator ArcLight using Lipofectamine (Invitrogen) following manufacturer's recommendations. Two to three days after transfection the coverslips were inverted onto ME films for testing. Preparation of GFP controls followed the same procedure with the exception of replacing the ArcLight vector (AddGene) with a GFP expression vector (AddGene). For experiments performed with cells grown on the films, HEK cells transfected with ArcLight were placed onto parylene coated poly-l-lysine treated films. The films were placed in cellular media overnight and tested the following day. The healthy proliferation of HEKs on the ME device indicates that this encapsulation approach prevents the ME materials from limiting cell growth (Figure S2B).

ArcLight and GFP were excited at 460 nm with an LED light source. Fluorescence images were collected at 33 fps using a CCD camera. Images were analyzed using MATLAB to quantify fluorescence changes in individual cells. *In vitro* testing was performed in extracellular buffer (ECB, in mM: NaCl 119, KCl 5, HEPES 10, $CaCl_2$ 2, $MgCl_2$ 1; pH 7.2; 320mOsm)

Figure S2B was obtained by growing unmodified HEK cells on a film submerged in cellular media for five days. The cells were then stained with Hoechst and Calcein-AM to label the nucleus and membrane respectively in living cells. The cells were then fixed and imaged using a confocal microscope.

Skull Phantom Demonstration

At the magnetic field frequencies used for this experiment bone and tissue are effectively transparent (Bottomley and Andrew 1978), so we selected a life sized skull with the size of an average human adult head as a phantom (Orient Infinity Limited). It was wrapped with 18 AWG magnet wire as shown in Figure 2. The coil consisted of four coils in parallel each wired to an individual magnetic field driver. All drivers were wired to the same input frequency signal and powered from the same power supply. The films were suspended at the center of the skull phantom. Orange LEDs (Chanzon) with a diode antiparallel were attached to the films for wireless verification of the voltage generated by the films. For visualization purposes the skull top was removed to better photograph the LED.

Two film biphasic circuit design

The first film is attached to a full wave rectifier, which is oriented to generate a positive pulse, while the second film is attached to a full wave rectifier that generates a negative pulse. These transistors block currents generated by one film from propagating through the circuitry attached to the other film, ensuring that only one half of the circuit is active at a time. We could also ensure that the positive and negative stimuli had equal amplitudes by independently adjusting the distance between each film and the permanent magnet.

Electrophysiology

We prepared thalamocortical brain slices (400 μm) as described previously (Agmon and Connors 1991). Briefly, wild-type mice were anesthetized and decapitated, in accordance with NIH guidelines and approved by the University of Texas Health Science Center at Houston (UTHealth) animal welfare committee. Brains were removed and immediately transferred to an ice-cold sucrose-based cutting solution containing (in mM): 234 sucrose, 2.5 KCl, 1.25 NaH_2PO_4, 10 $MgSO_4$, 0.5 $CaCl_2$, 26 $NaHCO_3$, and 11 glucose, saturated with 95% O2, 5% CO_2. Slices were cut using a vibratome (Leica VT 1200S) and transferred to ACSF containing (in mM): 126 NaCl, 2.5 KCl, 1.25 NaH_2PO_4, 2 $MgCl_2$, 2 $CaCl_2$, 26 $NaHCO_3$, and 10 glucose. Slices were held at 35°C for 20 min and then kept at room temperature until used for recordings. For experiments, slices were placed in a recording chamber and perfused with ACSF held at 31-34°C and containing NBQX (R&D Systems) to block AMPA receptor-mediated synaptic transmission. Whole-cell voltage-clamp recordings from neurons in the thalamic reticular nucleus (TRN) were performed using glass pipettes (3-5 MΩ) filled with a potassium based internal solution containing (in mm): 133 K-gluconate, 1 KCl, 2 $MgCl_2$, 0.16 $CaCl_2$, 10 HEPES, 0.5 EGTA, 2 Mg-ATP, and 0.4 Na-GTP (adjusted to 290 mOsm, pH 7.3). Antidromic action potentials were evoked by placing stereotrodes in the adjacent ventrobasal nucleus of the thalamus. Data were acquired using a Multiclamp 700B amplifier (Molecular Devices), filtered at 10 kHz, and digitized at 20 kHz with a 16-bit analog-to-digital converter (Digidata 1440A; Molecular Devices).

GCaMP Imaging

Brain slices were prepared closely following procedures described previously (Ting et al., 2014). GAD2-GCaMP3 mice were deeply anesthetized with Isoflurane and perfused with ice cold NMDG-based solution consisting of (in mM): 92 NMDG, 2.5 KCl, 1.25 NaH_2PO_4, 10 $MgSO_4$, 0.5 $CaCl_2$, 30 $NaHCO_3$, 20 glucose, 20 HEPES, 2 thiouera, 5 Na-Ascorbate, 3 Na-pyruvate, saturated with 95% O_2 and 5% CO_2., at a rate of ~6 ml/min. Coronal brain slices (300 μm) were cut using a vibratome (Leica VT1200S), incubated for 15 min at 35°C in NMDG-based solution, and then transferred to a chamber held at room temperature containing (in mM): 92 NaCl, 2.5 KCl, 1.25 NaH_2PO_4, 2 $MgSO_4$, 2 $CaCl_2$, 30 $NaHCO_3$, 25 glucose, 20 HEPES, 2 thiouera, 5 Na-Ascorbate, 3 Na-pyruvate, saturated with 95% O_2 and 5% CO_2. For experiments, slices were placed into a recording chamber perfused with ACSF containing (in mM): 126 NaCl, 2.5 KCl, 1.25 NaH_2PO_4, 2 $MgCl_2$, 2 $CaCl_2$, 26 $NaHCO_3$, 10 glucose), held at 32-34°C. The AMPA receptor antagonist NBQX

(10 μM) was included in the bath solution to block synaptically mediated network activity. Stereotrodes were placed in layer 5 of somatosensory (barrel) cortex. GCaMP3 expressed in GAD2 positive GABAergic neurons was excited at 460 nm with an LED light source. Fluorescence images were collected at 9.8 fps using a CCD camera attached to an Olympus BX51WI microscope equipped with a 60x water immersion objective. Images were analyzed using MATLAB to quantify fluorescence changes from a 300 × 300 μm region around the stereotrode tips.

Rat Surgical Procedures

All experiments were approved by the Rice University Institutional Animal Care and Use Committee's guidelines and adhered to the National Institute of Health guidelines. For both rotation tests and place preference animal experiments a total of six male Long-Evans rats (three per experiment weighing in the range of 500-800 g) were anesthetized with isoflurane gas. Five percent isoflurane was used to induce anesthesia and 1.5%–2.5% was used to maintain anesthetic depth. Buprenorphine (0.04mg/kg) was administered prior to ear bars as an analgesic. Following initial setup surgical methods differ for the two experimental protocols. For rotation test experiments, 5-7 skull screws were placed to anchor the electrode array. Skull screws were bound to skull with C&B Metabond (Parkell). A craniotomy was made to accommodate the microelectrode array and expose an injection site for neurotoxin. A 30-gauge needle was bent at the tip to pull away dura covering the brain. Desipramine (DMI) reconstituted in saline at a concentration of 15 mg/mL was injected IP to protect noradrenergic neurons. The dose of DMI was approximately 15 mg/kg and injected approximately 30 minutes prior to administration of neurotoxin. To induce a hemiparkinsonian lesion, 8 ug of 6-hydroxydopamine (OHDA) at 2ug/uL in saline was injected at 0.2 uL/min into the medial forebrain bundle (MFB −1.2mm–-1.25mm ML, −4mm AP and −8.1mm DV). STN stimulation was delivered via 2x2 platinum iridium microelectrode array (Microprobes) with 600 × 600 um spacing of 75 um electrodes. Each electrode had a nominal 10 kOhm impedance. For two rats electrode array was lowered to −2.6mm ML, −3.6mm AP and −8.2mm DV from bregma. For the third rat the electrode array was placed into the brain at 2.5mm ML, −3.4mm AP relative to bregma and −7.7mm DV relative to dura. The array was fixed to the skull with standard two-part dental acrylic. For place preference experiments 3-4 skull screws were placed above bregma. Skull screws were similarly bound to the skull with Metabond dental acrylic; however, the Metabond acrylic was limited to flow only above bregma. A craniotomy and duratomy above the location of the MFB (−1.8mm ML, −2.8mm AP) was made to accommodate for a 9 mm platinum iridium bipolar stereotrode from Microprobes with a nominal 10 kOhm impedance at 1 kHz. A custom 3D printed rounded/smoothened enclosure housing the electronics and connecting to the stimulating electrode was stereotactically lowered into the exposed brain to the depth of the MFB at −8.6mm–8.7mm DV relative to bregma. Kwiksil from World Precision Instruments was injected into the duratomy site built up to the base of the housing. Metabond was then applied again to the base of the 3D printed housing down to the Metabond on the skull screws. For a final securing of the implant, UV curing Flow-IT (Pentron) was used to cover the implant and anchor it to the Metabond in order to avoid the heat generated from the curing of standard two-part dental acrylic from damaging the custom housing and electronics. Lastly, the animal skin was sutured over the implant leaving it enclosed underneath the skin. The sutures were found to be strongest and confirmed to hold for at least one month when using minimal (1–2) interrupted sutures over the implant itself.

Hemi-Parkinsonian Experiments

Prior to stimulating each rat with the magnetoelectric stimulator, the stimulator power was estimated via a benchtop approximation of the rodent electrode impedance. Constant current stimulation of the rodent brain with an A-M Systems 4100 stimulator produced characteristic voltage waveforms that approximated a simplified parallel RC circuit. A 56 kOhm resistor, and 440 pF capacitor in parallel closely approximated the impedance characteristics of the rat brain across the stimulating electrodes. Using this circuit model, we estimated the field strengths and pulse durations necessary to produce the desired stimulation effects and confirm that the stimulation was charge balanced prior to rodent experimentation.

Prior to performing the rotation tests the rat was briefly anesthetized with 5% isoflurane gas and injected intraperitoneally (IP) with methamphetamine (0.31 mL 1.25 mg/kg) and the wireless biphasic stimulator was plugged into the implanted electrode array. After the anesthesia had worn off (about 5-10 min) the rat was placed in the cylindrical behavioral chamber. The magnetic field was applied over the whole behavioral area to the films on the device (Figure S5A).

The magnetic field was applied on resonance and off resonance for one minute at various times during the 40-minute trial. The resonant frequencies were 130 kHz and 160 kHz and the off resonant frequencies were 120 kHz and 170 kHz.

Rodent Tracking

Head position on the rotation task was generated using a version of DeepLabCut (Mathis et al., 2018) to track ears, snout, and implant. A dataset totaling 286 frames from both the on and off resonance rotation tasks was hand labeled and trained for approximately 140,000 iterations.

Position during both behavioral tasks was also manually tracked via custom python scripts. The overall place preference was quantified by counting the number of frames in which the animal was inside either one of the coils.

Place Preference Implant Design

The miniature ME films were fabricated from PZT/Metglas. The circuit components used were the same as those used in the brain slice and rotation test, however in this case there was no circuit board and the elements were soldered together directly and the films

attached with conductive epoxy. The films/circuit were parylene coated for extra insulation and then a small bias magnet was attached in the orientation and position that ensured the best charge balance between the two phases. The plastic case designed to put the least stress on the skin was 3D printed in plastic and included a channel to securely hold the stereotrode and a chamber to hold the circuit/films. The circuit/films were attached to the stereotrode with conductive epoxy and a combination of Flow-It ALC (Pentron) and epoxy were used to encapsulate the entire outside of the box. Prior to implantation the implant was put through a 12 hour ethylene oxide cycle followed by a 12-24 hour degas period inside of a fume hood.

Place Preference Experiments

The rats were given a minimum of 24 hours to recover. We performed the experiments 1-3 days after the surgery. The rat was placed on a linear track with a coil at each end. Both coils applied a resonant alternating magnetic field, but only one was on resonance to activate the implanted device. We took a 10 minute video recording of the rat position starting from the first time the rat received stimulation from the ON resonant coil. After 10 minutes the rat was removed from the track and placed back into the home cage for a minimum of 5 minutes while the track was cleaned. In order to ensure that the rat did not develop associations with specific places in the room, we rotated the track to an arbitrary angle between each of the six trials. In total we performed 6 trials/rat. Between the third and fourth trial the system was also re-tuned to switch which coil was resonant with the device in addition to rotating the track.

QUANTIFICATION AND STATISTICAL ANALYSIS

Error bars in Figure S1M denote ± one standard deviation for n = ~50 data points, n refers to an individual film. We furthermore performed a Tukey's Honest Significant Difference test on the data in Figure S1M, which indicated that the voltage produced at each different PVDF thickness is significantly different.

Paired t tests were used for the rodent tests in Figures 4 and 5. Star values indicate levels of significance associated with the P values listed in the figure captions. In Figure 4F we compared n = 9 data points for before and during off resonance stimulation and n = 9 data points for before and during on resonance stimulation where n refers to 1 stimulation period during a trial. In Figure 4G we compared n = 29 for on resonance data points and n = 28 for off resonance data points, where n refers to all the rotation rate data points for all rats during the specified time periods (averages for each rat shown in figure, not individual data points). In Figure 5F we compared n = 3 data points for each coil during a trial, where n = amount of time spent in one coil compared to the other. In Figure 5G we compared n = 9 data points (averages for each rat shown in figure, not individual data points) where n = individual data points for amount of time spent in one coil during a trial. The supplemental power analysis was done using MATLAB to estimate a sample size based on potential means and standard deviations of a larger dataset from our proof of principle work. Values used in the estimate were as follows: Rotation test: means = 11 and 6 rpm, standard deviation = 4. Place preference test: means = 70 and 30%, standard deviation = 20.